This document is the accepted manuscript version of the following article:
Yang, S. C., Lin, T. Y., Ochoa, M., Lai, H., Kothandaraman, R., Fu, F., … Carron, R. (2022). Efficiency boost of bifacial Cu(In,Ga)Se2 thin-film solar cells for flexible and tandem applications with silver-assisted low-temperature process. Nature Energy. https://doi.org/10.1038/s41560-022-01157-9

Efficiency boost of bifacial $Cu(In,Ga)Se_2$ thin-film solar cells for flexible and tandem applications with silver-assisted low-temperature process

Shih-Chi Yang[1], Tzu-Ying Lin[2], Mario Ochoa[3], Huagui Lai[1], Radha Kothandaraman[1], Fan Fu[1], Ayodhya N. Tiwari[1], and Romain Carron[1]*

E-mail: shih-chi.yang@empa.ch

[1]Laboratory for Thin Films and Photovoltaics, Empa - Swiss Federal Laboratories for Materials Science and Technology, Dübendorf, Switzerland
[2]Department of Materials Science and Engineering, National Tsing Hua University, Taiwan
[3]Photonics Engineering Group, University of Cantabria, Santander, Spain

Abstract

Bifacial $Cu(In,Ga)Se_2$ thin-film solar cells are attractive for a wide range of applications; however, low power conversion efficiencies of bifacial $Cu(In,Ga)Se_2$ devices is a severe limitation. Significant enhancement requires new approaches to prevent GaO_x formation at the back interface and improve the carrier collection under rear illumination. In this contribution, we take advantage of silver-promoted low-temperature growth process to completely remove GaO_x formation at back interface while enabling high absorber quality, steep Ga back gradients and less absorption in transparent back contacts. We report a certified cell on a glass substrate with record efficiencies of 19.77% and 10.89% under front and rear illumination. Moreover, direct fabrication of bifacial $Cu(In,Ga)Se_2$ solar cells on flexible substrates is demonstrated for the first time. Finally, we report the first bifacial perovskite/$Cu(In,Ga)Se_2$ tandem solar cell in a 4-terminal configuration, achieving power generation densities of 27.0 mW/cm² $BiFi_{200}$ and 28.0 mW/cm² $BiFi_{300}$, respectively.

The goal of limiting global warming to 1.5°C above pre-industrial levels and reducing greenhouse gases to net zero by 2050 is well-recognized.[1] Photovoltaics (PV) is expected to play an important role in facilitating the transition to a low-carbon economy, mitigating climate change, and meeting energy demands.[2] PV market has grown rapidly, and between 2008 and 2020 global solar PV power generation increased from 11.9 TWh to 821 TWh.[3] Compared with conventional monofacial-based PV systems, bifacial PVs have a strong potential to obtain higher annual energy yield thanks to the extra light reflected or diffused to the rear side. The benefits are especially attractive in applications such as building-integrated photovoltaics (BIPV),[4] vertically mounted bifacial PV (VBPV),[5] and agrivoltaics,[6] which offer both low-carbon emission and low levelized cost of electricity (LCOE).[7,8] According to the International Technology Roadmap of PV (ITRPV), bifacial PV could capture 40% of the PV market by 2028.[8,9]

Si wafer based bifacial PV has reached industrial maturity and is widely used, while some preliminary research efforts have been made for bifacial thin-film solar cells. Unfortunately, the power conversion efficiency (PCE) of bifacial Cu(In,Ga)Se_2 (CIGS) thin-film solar cells has remained rather low whereas mono-facial CIGS cells with record PCE of 23.35%[10] and 21.4%[11] have been achieved on rigid glass and flexible polymer substrates, respectively. The highest PCE under one sun rear illumination doesn't exceed 7.1% and its PCE under front illumination is just 9.0%.[12] As a consequence, bifacial CIGS solar cells and their various applications are still unattractive despite their great potential.

To collect the sunlight from the rear side, a transparent conductive oxide (TCO) is required to replace the conventionally used opaque Mo back contact in the mono-facial configuration. However, the detrimental GaO_x is commonly formed at the CIGS/TCO interface during high-temperature growth process for absorber deposition. GaO_x is highly resistive and may form a reverse, second p-n junction at the back contact, which deteriorates especially the fill factor (FF).[13,14] Many efforts have been dedicated to suppressing GaO_x formation, but none of them were successful when it comes to device performance.[14–16] The highest reported PCE with TCO back contact under front illumination is limited to merely 16.1%.[16] Therefore, the development of TCO-based devices including bifacial, semi-transparent, and ultra-thin rear-back-contact (RBC) devices remained stagnant.

Very low PCEs under rear illumination in bifacial CIGS devices are attributed to short diffusion length of carriers and high rear interface recombination. Commonly introduced Ga back gradient in CIGS absorbers can suppress the back interface recombination,[17] but the required high Ga content results in poor absorber quality, and aggravates the formation of GaO_x interlayer. Moreover, the high-temperature CIGS deposition process also prevents strong Ga gradients due to increased elemental inter-diffusion. As a result, the bifaciality in CIGS devices is usually low. The use of ultra-thin absorbers can slightly mitigate the problem by extending the space-charge region to the back interface, but the PCEs are strongly compromised because of incomplete absorption of photons and higher impact of back interface recombination.

Recently, silver-alloyed CIGS has shown better material properties as compared to CIGS, such as larger grain sizes,[18] fewer structural defects, and less sub-bandgap disorder,[19] which

are connected to a lower melting point[20] and enhanced elemental inter-diffusion.[21] Previously, we have reported that silver can widen the absorber deposition temperature window of high performance CIGS solar cells.[22] By adding a small amount of Ag, high-quality absorbers can be obtained with a low-temperature process down to 300°C. Such low-temperature deposition opens the possibility of suppressing the formation of GaO_x while simultaneously building up strong Ga gradients. Herein, we take advantage of the silver-promoted low-temperature process to completely remove GaO_x formation at the CIGS/ITO interface while keeping high absorber quality, and steep back bandgap gradient. Our strategy enables the development of a CIGS bifacial solar cell with a certified efficiency of 19.77% and 10.89% under the front and rear one-sun illumination, respectively. These efficiencies correspond to a significant boost compared to existing reports. Finally, we present different bifacial devices including flexible bifacial and bifacial perovskite/CIGS tandem devices as proof-of-concepts, paving the way for future developments of the next generation of bifacial thin-film tandem devices.

Reduction of CIGS deposition temperatures on ITO

Our approach involves deposition of a 15 nm-thin Ag precursor layer on soda-lime glass (SLG) covered with a SiO_x alkali diffusion barrier and 200 nm indium tin oxide (ITO) layer. A modified multi-stage coevaporation[23] process was used in order to maximize GGI ([Ga]/([Ga]+[In])) near the back interface of the 2 μm thick absorber. The amount of Ag in the absorbers corresponds to about 4-5% AAC ([Ag]/([Ag]+[Cu])) ratio. NaF and RbF post-deposition treatment (PDT) were applied in-situ.[22,23] The sample fabrication is described in Section **Methods**. The device structure of bifacial CIGS solar cells is schematically illustrated in **Fig. 1a**. To investigate the GaO_x interlayer formation at different substrate temperature, CIGS deposition were performed at four different nominal substrate temperatures (T_{sub}) from 453°C to 303°C, with corresponding sample names T453, T413, T353 and T303. The GGI depth profiles obtained from time-of-flight secondary ion mass spectrometry (SIMS) for those absorbers are shown in **Fig. 1b**. Higher T_{sub} enhances elemental inter-diffusion, and significantly reduces Ga back gradient, especially for T453, with a ΔGGI of only 0.3. On the contrary, both T303 and T353 have ΔGGIs of around 0.6.

CIGS/ITO interface was carefully investigated by STEM (scanning transmission electron microscopy) and EDS (energy-dispersive X-ray spectroscopy) to find the presence or absence of GaO_x interlayer in the different samples. **Fig. 1c** and **Fig. 1d** show EDS mappings of Ga and O signals for samples T453 and T353. High Ga signal at the interface was detected in T453, but not in T353. EDS line scans of Ga and O across the interfaces are provided in **Fig. 1e** and **Fig. 1f**. A 2-5 nm-thick GaO_x interlayer is present at the CIGS/ITO interface of T453, confirmed by the Ga accumulation and the early O signal increase. As for T413, a very thin GaO_x interlayer (1-2 nm) is still present, as shown in **Supplementary Fig. 3**. In contrast, no interlayer could be evidenced in T353, convincingly suggesting the low temperature CIGS deposition is effective to reduce/avoid the formation of GaO_x interlayer.

Fig. 1g and **Fig. 1h** show bright-field and dark-field STEM images for samples T453 and

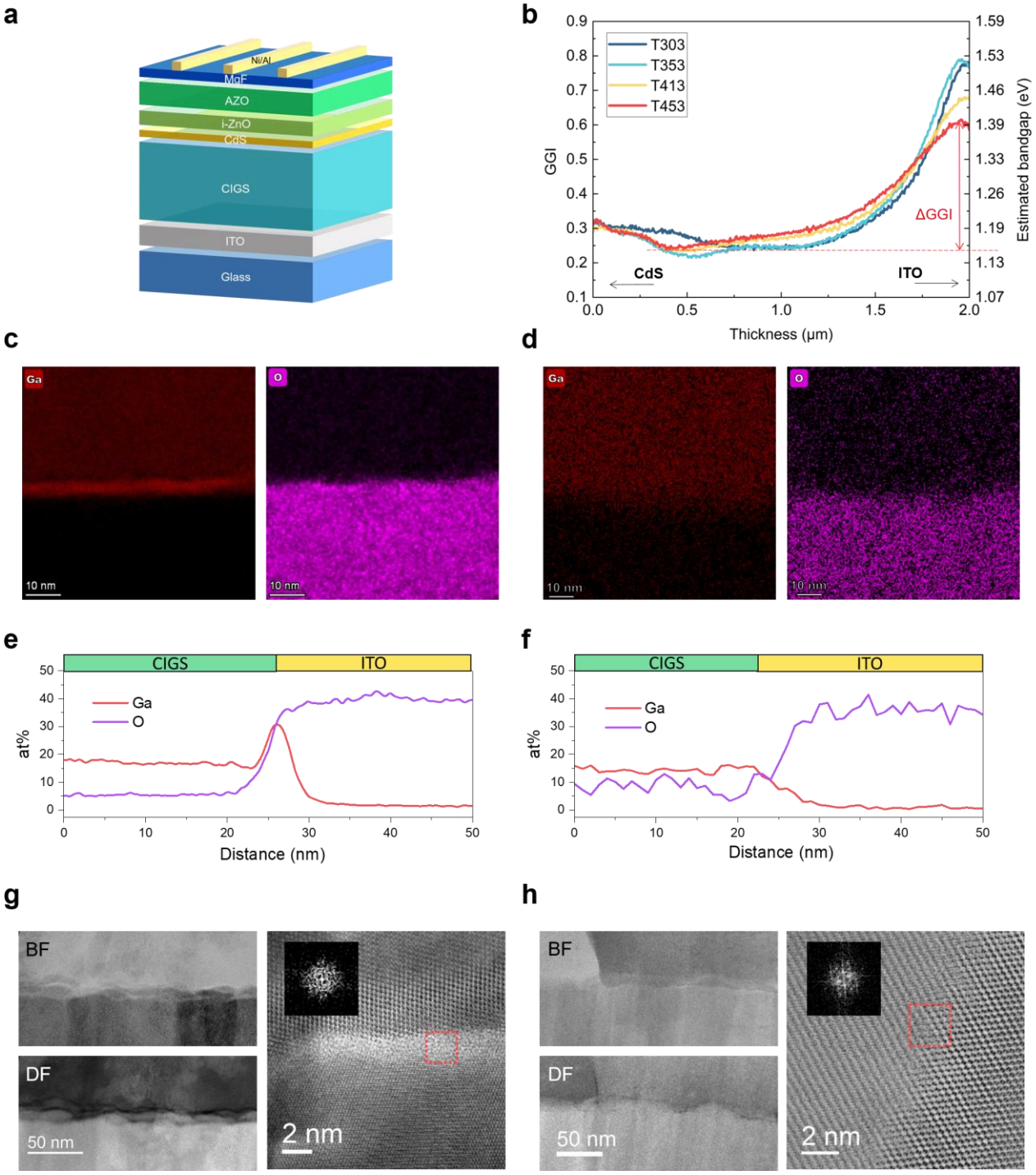

Figure 1: Experimental design and material analysis at CIGS/ITO interface. (a) Device structure of the bifacial CIGS solar cells on glass substrates. (b) GGI and bandgap depth profiles of the absorbers grown at different temperatures. (c) EDS mapping of Ga and O for T453, and (d) for T353. (e) EDS linescans of Ga and O across the interface for T453, and (f) for T353. (g) Bright-field and dark-field STEM images near the CIGS/ITO interface of T453, and (h) of T353, together with high resolution images of the interface region including FFT of the evidenced interface area.

T353. High resolution bright-field images and the fast Fourier transform (FFT) of the evidenced areas near the interface are also provided. In T453, an amorphous interlayer is evidenced with

a thickness of around 2 nm. Instead, high resolution STEM of T353 reveals a sharp interface between ITO and CIGS. Crystallized phases with specific orientations are present on the two sides of the interface. The corresponding FFT around the interface also supports this observation. Therefore, we conclude that low T_{sub} effectively suppresses the GaO_x formation despite very high GGI (about 0.8, as shown in **Fig. 1b**) near the back interface. It enables building up a stronger effective electric field with pronounced Ga gradients while avoiding formation of undesired GaO_x. In addition, the SiO_x barrier layer used in those absorbers might also play a role in reducing GaO_x since the presence of Na during absorber growth can promote the GaO_x formation.[24]

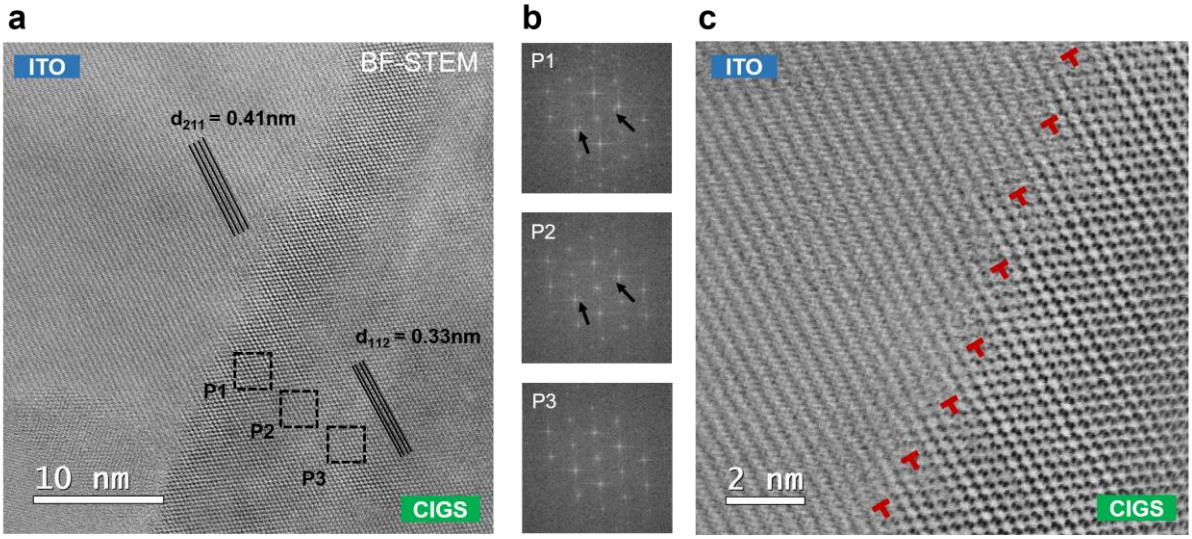

Figure 2: Misfit dislocations in CIGS near CIGS/ITO interface. (a) Bright-field STEM image near the CIGS/ITO interface of sample T353. The crystal orientation of both ITO and CIGS layers are labeled. (b) FFT of areas P1, P2 and P3 showing additional diffraction points disappearing at some distance from the interface. (c) Misfit dislocations with alternating distances ($5\times d_{112}$ and $4\times d_{112}$) evidenced in the CIGS, near the ITO/CIGS interface.

Due to the absence of GaO_x interlayer in T353, we observe not only local expitaxy of CIGS on ITO back contacts but also "misfit dislocations" on CIGS to accommodate the lattice mismatch between ITO and CIGS, as shown in **Fig. 2**. During the growth of CIGS absorbers, dislocations form to reduce the total energy as the strain energy increases with absorber thickness. By considering the mismatch of (211) interplanar spacing (d-spacing) in ITO layer (about 0.41 nm) and (112) d-spacing in CIGS (about 0.33 nm), the observed alternating distances between misfit dislocations (5 and 4 atomic spacings) near the interface are well explained by **Eq. 1**. One period ($9\times d_{112}$) on CIGS side is equivalent to $7\times d_{211}$ in ITO. These observation hints at the possibility of epitaxial CIGS deposition on ITO substrates with GaO_x free interface, for example to trigger formation of CIGS layers with large grains.

$$d_{\mathrm{ITO\ (211)}} \times 7 = 2.87nm \approx 2.97nm = d_{\mathrm{CIGS\ (112)}} \times 9 \qquad (1)$$

Efficiency limiting factor under front illumination

CIGS solar cells with Mo back contact usually yield higher PCE owing to better material quality with increased T_{sub}.[22,25] However, for our CIGS solar cells on ITO back contact, we identified an optimal T_{sub} for highest PV performance. **Fig. 3a** shows the the current–voltage (J-V) curves under front illumination for samples T303, T353, T413 and T453. Sample T353 yields the best PCE of 17.7% without noticeable current blocking, while a mild blocking behavior starts to appear in T453. With higher T_{sub}, FF limits the device efficiency due to higher apparent series resistance (R_s). We attribute the difference to the formation of the highly resistive GaO_x interlayer. Owing to their band alignment, the p-CIGS/n^+-ITO interface is supposed to form a Schottky, reverse diode contact. In absence of GaO_x interlayer like in T353, it was postulated that easy charge transport can occur through the Schottky barrier by trap-assisted tunneling of holes mediated by Na-induced defects near the interface, as illustrated in **Supplementary Fig. 6**.[13,15,26] In turn, GaO_x is assumed to be a highly resistive n^+ material with a large valence band edge offset to CIGS. Therefore the existence of a GaO_x interlayer should considerably increase the height of the hole barrier and hinder the charge transport. This explains why the presence of GaO_x at interface can play a crucial role in FF and device performance under front illumination. However, it is worth noting that good FF might still be achieved[16] by changing the properties of GaO_x or different supply of Na. Also, the coverage and thickness uniformity of GaO_x can also play a role. While the above mentioned factors strongly depends on different group's equipment, process and so on and are more difficult to control and reproduce in different research groups, we believe our strategy of complete removal of GaO_x is more robust.

On the other hand, reduced deposition temperature of 303°C degrades the absorber quality and increases open-circuit voltage (V_{OC}) deficit, despite a slightly higher FF (see PV parameters in **Supplementary Table 1**). We further performed EQE measurements as shown in **Fig. 3b**. The samples show quite similar response, except for slightly reduced EQE response at long wavelengths for sample T303. This decrease can be understood by the degraded absorber quality and worse collection of charge carriers. Due to the trade-off between absorber quality for high V_{OC} and the formation of GaO_x limiting FF, sample T353 yields the best PCE under front illumination.

To bridge the PCE gap with Mo-based devices, we further optimized the amount of RbF PDT and CGI composition ratio ([Cu]/([Ga]+[In])). It is well-known that such optimizations are important for V_{OC} and device performance[27] improvement. **Fig. 3c** shows samples with higher CGI and optimized RbF with the lowest V_{OC} deficit achieved (about 410 mV). Finally, we minimized the contact resistance to compensate for the high sheet resistance of the 200 nm-thick ITO (about 10 ohms per square) by applying a conductive paste directly around the cell area. The best cell yields 19.7% under front illumination, very similar to baseline process for cells using Mo contact. Hence, we demonstrate solar cells with ITO back contact with almost no additional loss as compared to their Mo counterpart.

To visualize the importance of Rs, we plot in **Fig. 3d** the PCE versus FF of individual cells of different samples, with the size of bubbles representing Rs values. The Rs values behave con-

sistently versus deposition temperature. It is clear that PCE is mainly driven by FF, and that Rs is the key limiting factor to high FF. To exclude that higher Rs might originate from degradation of ITO during CIGS deposition, we measured the sheet resistance (R_{sheet}) of ITO before and after CIGS deposition, by mechanically removing of all layers above ITO in finished devices (see **Supplementary Table 3**). R_{sheet} of ITO is almost unchanged upon absorber deposition for all investigated T_{sub}, although its optical properties are degraded as described below.

Efficiency limiting factor under rear illumination

Fig. 4a shows the J-V curves of bifacial CIGS solar cells under 1-sun rear illumination. As for front illumination, sample T353 yields the highest PCE, mainly due to higher J_{SC}. The other PV parameters are in reasonable agreement with measurements from the front side (see **Supplementary Table 2**). EQE measurements under rear illumination are provided in **Fig. 4b**.

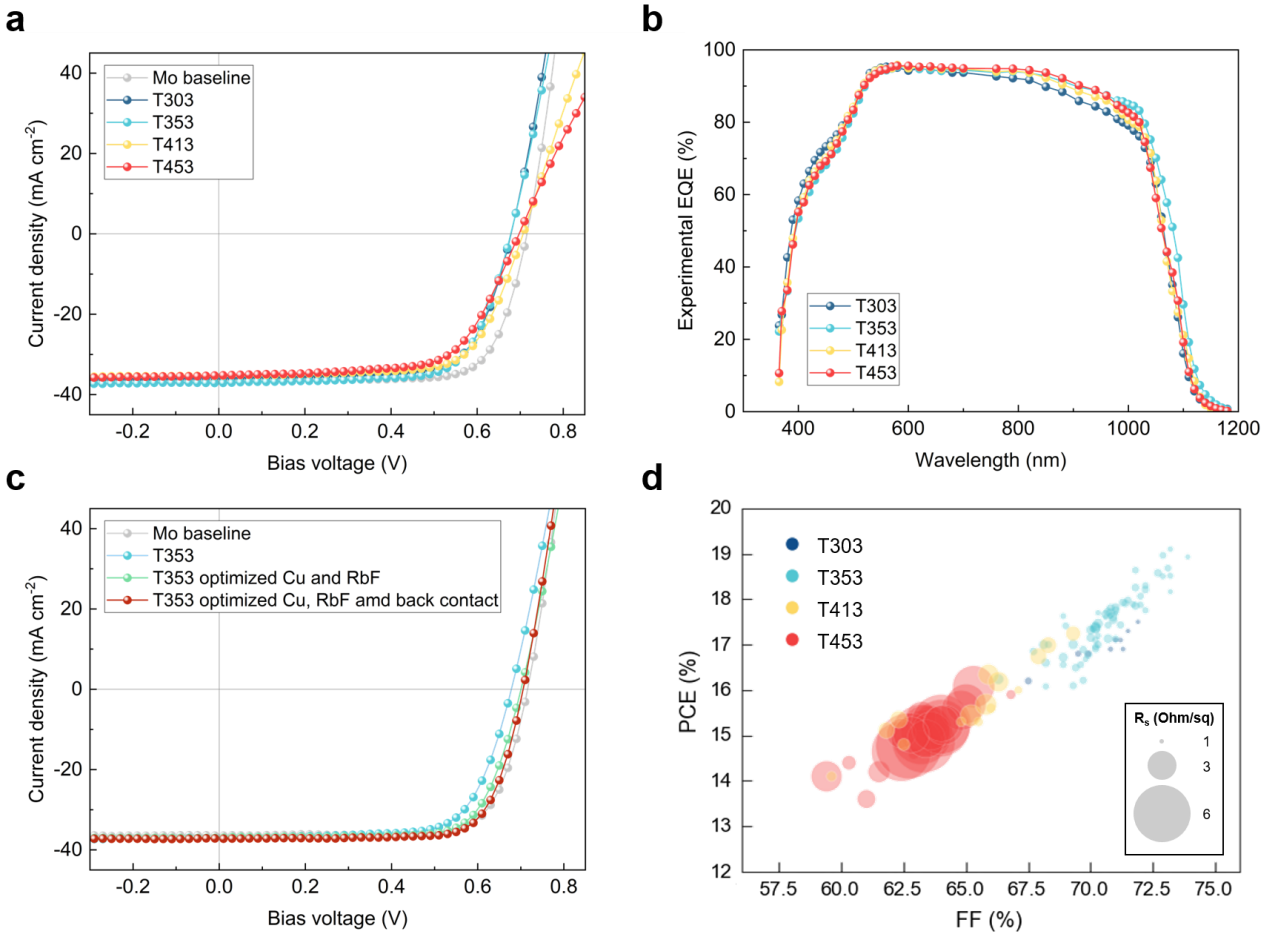

Figure 3: Photovoltaic performance characterization under front illumination. (a) J-V curves of bifacial CIGS solar cells grown at different T_{sub} under one sun front illumination. (b) Corresponding EQE curves. (c) J-V curves of bifacial cells grown at 353°C under one sun front illumination, after optimization of deposition and cell processing (see text). (d) R_s bubble chart with respect to PCE and FF. All the samples fabricated in this study are included.

The low EQE response at short wavelengths is mainly due to back interface recombination and short photon penetration depth.[28] Below we investigate the EQE response at long wavelengths. We measured the cell back reflectance R_{back} (**Supplementary Fig. 5**, little differences), and the absorptance of ITO/SLG A_{ITO} after mechanical removal of absorber and front window layers (**Fig. 4c**). Then, we calculated the internal quantum efficiency (IQE) as $EQE/[(1-R_{back})(1-A_{ITO})]$ shown in **Fig. 4d**. Despite similar and unchanged ITO R_{sheet} values after CIGS deposition, the ITO optical parasitic absorption increases with higher T_{sub}. The root-cause is not clear yet, however it can be speculated that the amount of oxygen vacancies in ITO may change during the high temperature CIGS deposition[29,30] in Se ambient.

In long wavelength range (> 950 nm), IQEs are similar except for sample T303, as shown in **Fig. 4d**. The lower IQE of T303 is explained by inferior absorber quality and is in line with the degraded long-wavelength EQE under front illumination (**Fig. 3b**). Below 950 nm, one observes a maximum in the IQE curves, followed by decreased values at shorter wavelengths. The peak wavelength depends on T_{sub}. Through optical transfer-matrix TMM simulations, we show that this behavior arises from recombination at the CIGS/ITO interface and depends on the absorber GGI gradient.

Fig. 4e and **Fig. 4f** shows the absorber gradients of samples T353 and T453, discretized into 20 nm-thick sublayers and colorized with the expected optical absorption of a 850 nm illumination from the back, using composition-dependent refractive indices.[31] At that specific wavelength, the GGI profile has a strong impact on the distribution of photogenerated carriers. For sample T353, photons with wavelength > 850nm are absorbed relatively deep in the absorber due to the locally high GGI and bandgap, and subsequently mostly avoid carriers recombination at/near the interface. In contrast, high T_{sub} reduces the bandgap near the back interface, resulting in significantly higher absorption near the back interface and more loss of photogenerated carriers for 850nm excitation.

We further calculate the IQEs in **Fig. 4g** from the optical simulations, defined as the numerically integrated optical absorption in all CIGS sublayers (i.e. assuming collection probability is unity). We introduce a 'dead zone' within a certain depth from the back interface, in which photogenerated carriers are considered lost due to fast recombination (collection probability zero).[32] This very simple model reproduces well the wavelength of the experimental IQE maximum, which is limited on the one side by incomplete absorption, and on the other side by carrier recombination at the back interface. The wavelength of the IQE maximum is primarily determined by the absorber bandgap at the back interface.

Further, we considered two different depths of the dead zone (150 nm and 80 nm). The simulations shown in **Fig. 4g** also reproduce qualitatively well the shape of the experimental IQE below 800 nm photon wavelength (**Fig. 4d**). The width of the dead zone can be correlated to the steepness of GGI back gradients. Steeper GGI gradients correspond to stronger effective electric field assisting electrons transport towards the front interface, therefore a narrower dead zone. With a narrower dead zone (steeper gradient), the IQE response at short wavelength range is improved thanks to better carrier collection. The collection at shorter wavelength in

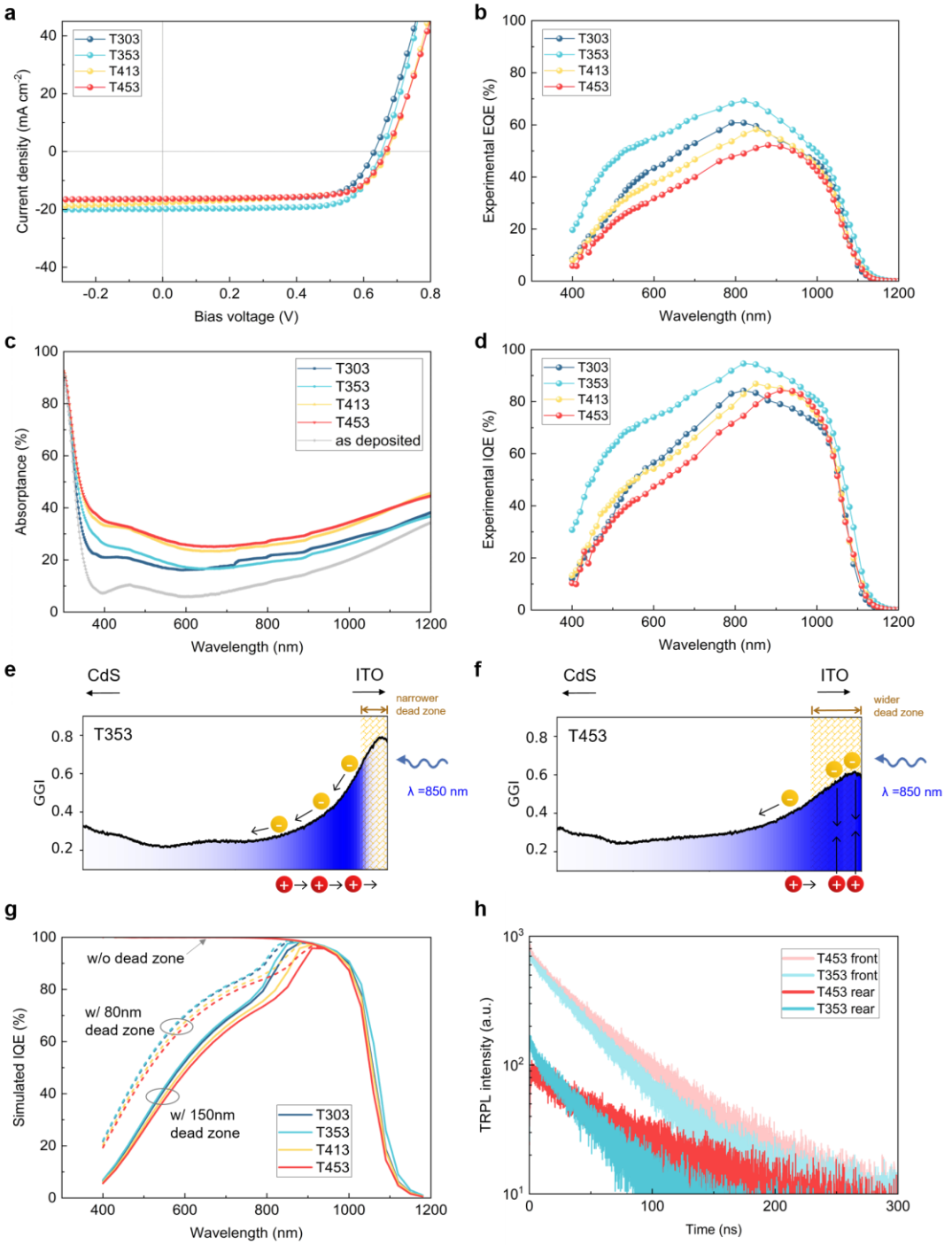

Figure 4: Photovoltaic performance under rear illumination. (a) J-V curves for bifacial CIGS solar cells grown at different T_{sub} under one sun rear illumination. (b) Corresponding EQE curves. (c) Absorptance of the ITO/SLG layers before and after CIGS deposition at different T_{sub}, after removal of CIGS and top layers. (d) IQE curves under rear illumination, accounting for cell reflectance and absorptance of the ITO back contact. (e), (f) Optical TMM simulations of the progressive absorption of an incident rear illumination with a wavelength of 850nm, as a function of absorber depth. The compositional gradients correspond to samples T353 and T453. (g) TMM optical simulations of IQE implementing experiemental gradients of the four samples, implementing a dead zone of different width near the rear interface. Carriers photogenerated in this dead zone are considered lost. (h) TRPL decays for T353 and T453 under front and rear excitation.

sample T353 is the best, whereas for sample T303 we expect inferior bulk absorber quality that degrades charge transport to the front interface despite a favorable GGI back gradient. Similarly as concluded from front illumination measurements, the absorber of T353 strikes a good balance between pronounced GGI back gradient and material quality.

Fig. 4h shows TRPL decays of T353 and T453 in low injection under front the rear illumination with a 635 nm pulsed laser. Measurements were performed after removal of the front TCO layer to prevent charge carrier extraction. In both configurations, T453 shows longer lifetime, in line with its smaller V_{OC} deficit and better bulk quality due to high T_{sub}. Under front excitation, T353 and T453 show similar intensities immediately after laser pulse, evidencing similar $\Delta n \times p_0$ product in the potential minimum (i.e. notch). Under rear excitation, T353 shows higher initial intensity than T453. It can be explained by higher Δn in the notch due to less absorption in ITO and suppressed recombination at the back interface in T353, in agreement with the IQE and absorptance value in ITO at the 635 nm wavelength.

Strategies to improve the short-circuit current

The main bottleneck limiting the PCE under rear illumination is the low J_{SC}. Therefore, we investigate and quantify the different current loss mechanisms and discuss strategies to improve J_{SC}. As shown in **Fig. 5a** and **Fig. 5b**, the highest loss arises from parasitic absorption in the ITO back contact. Less degradation in optical transparency of ITO after CIGS growth in T353 accounts for a maximum current gain of 3.5 mA/cm^2 (assuming unity collection and no parasitic absorption). Further efforts are needed to tune the ITO deposition process to minimize degradation of optical transparency during CIGS deposition. Replacing ITO with IO:H or IZO could help reducing the optical absorption while maintaining similar R_{sheet}.[33] The advantages of silver promoted low-temperature process should be transferable to other TCOs. The second highest loss of J_{SC} stems from uncollected (recombined) carriers. Mitigating the recombination at the back could be done by a steeper back gradient or by inserting a rear passivation layer[17] which has to be developed. Compared with T453, a current gain of 4.4 mA/cm^2 was obtained with more pronounced back gradient in T353. Last but not least, J_{SC} loss from the back reflection can be reduced by optical management strategies. An anti-reflection layer on the backside of glass, and interlayer such as a thin Al_2O_3 between ITO and glass may provide further J_{SC} increases.

Champion bifacial device with a significant PCE boost

A bifacial CIGS solar cell was obtained with efficiencies of 19.77% and 10.89% under front and rear one sun illumination, as independently certified by Fraunhofer ISE (**Fig. 6a**). To the best of our knowledge, both values are the highest efficiencies reported for bifacial CIGS devices. Usual strategies used up to now relied on absorber thinning ($\leq$ 1000 nm) to bring the space-charge region closer to the front interface, which in turn sacrifices the PCE under front illumination. (See Supplementary Fig. 4) Our results demonstrate an alternative design leading to high performance

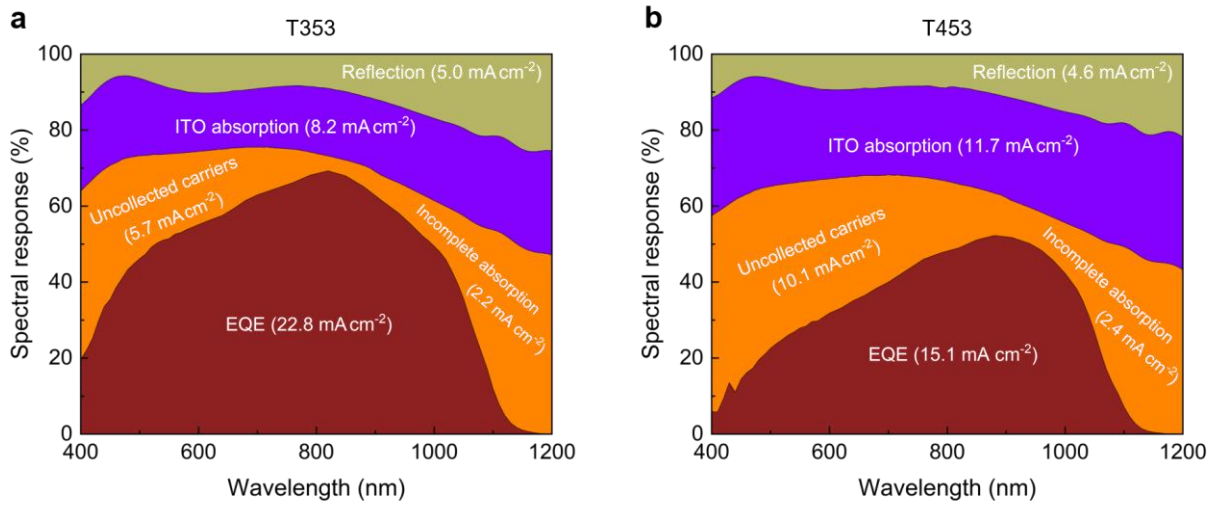

Figure 5: J_{SC} loss analysis. (a) Optical and J_{SC} loss analysis for sample T353 under rear illumination. (b) Analysis for sample T453. The loss mechanisms considered are reflection at the back, ITO absorption, uncollected carriers and incomplete optical absorption in CIGS. The J_{SC} losses are calculated in the wavelength range from 365 nm to 1150 nm. The 900 nm wavelength was chosen as the boundary for J_{SC} loss calculation between uncollected carriers and incomplete absorption.

under both front and back illumination. Under 30% albedo (average albedo considering different ground surfaces), a power generation density of 23.0 mW/cm² $BiFi_{300}$ is foreseen.

Potential for different bifacial device architectures

Upon the demonstration of high efficiency CIGS bifacial solar cells on a glass substrate, we explore two different device architectures as proof of concepts, namely bifacial CIGS solar cells on flexible substrates and 4-terminal perovskite/CIGS tandem solar cells.

To the best of our knowledge, all reported flexible bifacial CIGS devices rely on a lift-off process,[34–38] which is not considered attractive from an industry perspective, especially for large area and roll-to-roll manufacturing process. For the first time, we directly deposited CIGS onto ITO-coated flexible substrates (polyimide). The polyimide foils we used have a yellow-brown appearance with a reasonable near-infrared transparency. J-V curves of the best cell are shown in **Fig. 6b**, with PCEs of 15.36% and 6.61% under front and rear illumination, respectively. It is worth mentioning that V_{OC} under front illumination is close to that on SLG substrate, evidencing comparable absorber quality. However, the shunting issue related to experimental difficulties in cell definition on the polyimide substrate at the early stage of development, seems to have stronger impact on V_{OC} under rear illumination. As compared to SLG substrate, J_{SC} under rear illumination is further degraded by the optical absorption in the polyimide substrate. Besides thinner polyimides, more transparent flexible substrates such as colorless polyimide (CPI) may be suitable candidates to improve J_{SC}.

In **Fig. 6c**, we compare our best results on glass and PI with the-state-of-the-art bifacial solar cells of different PV technologies.[12,13,28,34–53] In the past, only silicon, perovskite and GaAs could reach simultaneously high bifaciality and high PCE. For high bifaciality, CIGS and CdTe always

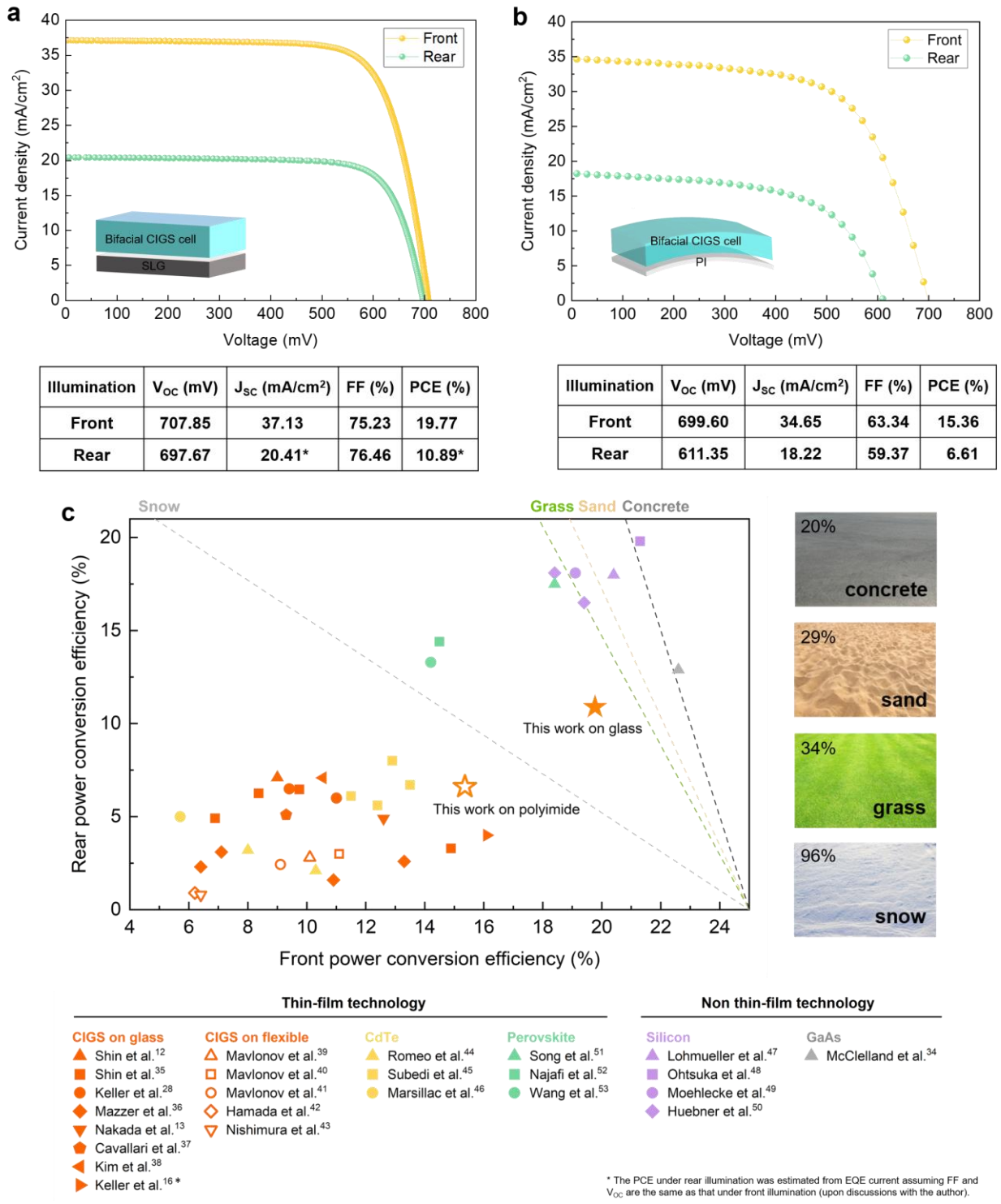

Illumination	V_{OC} (mV)	J_{SC} (mA/cm²)	FF (%)	PCE (%)
Front	707.85	37.13	75.23	19.77
Rear	697.67	20.41*	76.46	10.89*

Illumination	V_{OC} (mV)	J_{SC} (mA/cm²)	FF (%)	PCE (%)
Front	699.60	34.65	63.34	15.36
Rear	611.35	18.22	59.37	6.61

Figure 6: Champion cells and comparison with state-of-the-art. (a) Certification results from Fraunhofer ISE. *Both J_{SC} and PCE under rear illumination are underestimated as an illumination mask area of 0.6247 cm² was used during certification while the actual cell area is 0.5629 cm². For in-house measurement, a PCE of 12% was reached. (b) J-V curves of a bifacial CIGS device on polyimide under front and rear illumination. (c) Comparison between this work and state-of-the-art bifacial solar cells.

The dash lines are corresponding to 25% bifacial efficiency calculated by: front PCE + rear PCE×albedo. The albedo values for different ground conditions are shown in the corresponding figures.

needed to trade off PCE. With the help of Ag and an optimal T_{sub}, we obtained significant boosts in PCEs for bifacial CIGS solar cells on both glass and PI substrates. Such efficiency boost may open pathways towards the implementation of CIGS bifacial solar cells for unexplored applications up to now.

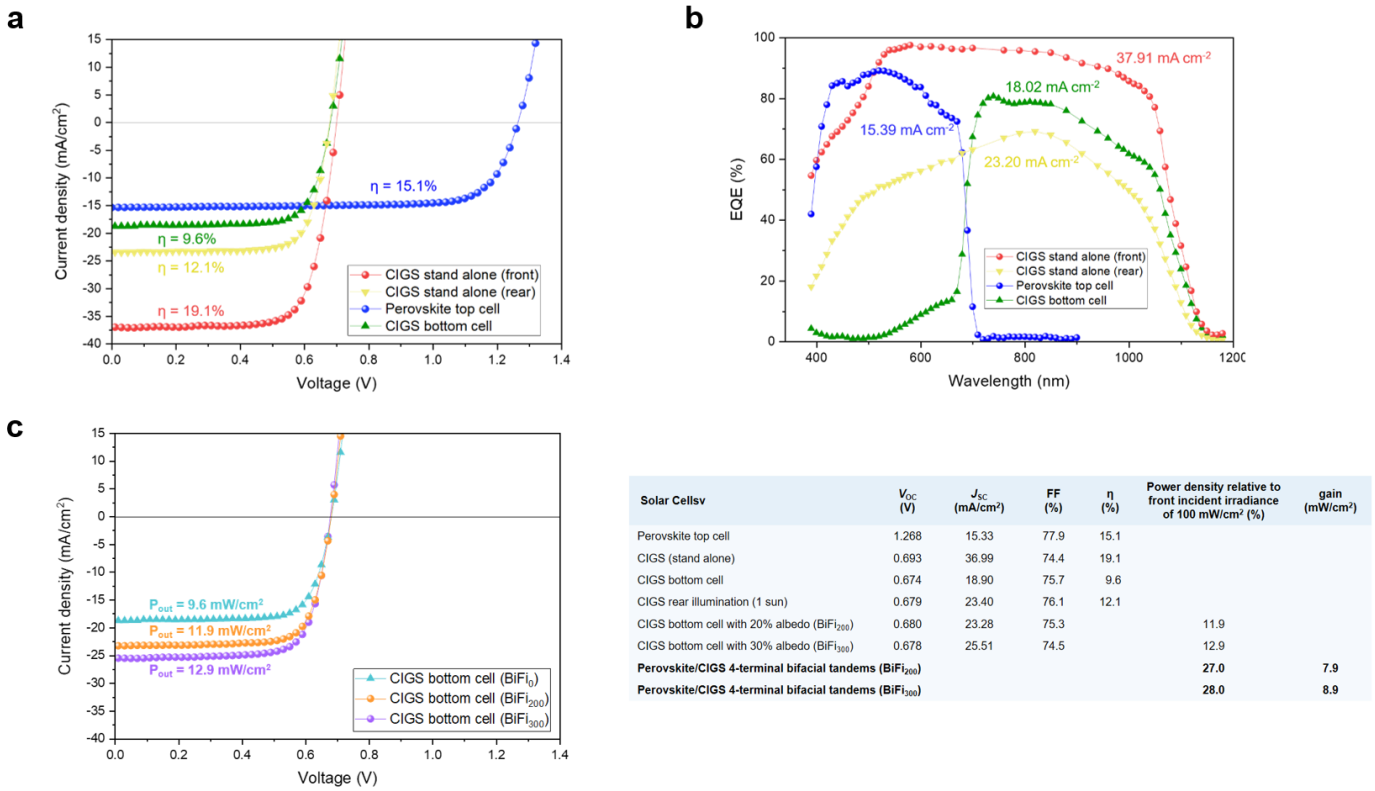

Solar Cellsv	V_{OC} (V)	J_{SC} (mA/cm²)	FF (%)	η (%)	Power density relative to front incident irradiance of 100 mW/cm² (%)	gain (mW/cm²)
Perovskite top cell	1.268	15.33	77.9	15.1		
CIGS (stand alone)	0.693	36.99	74.4	19.1		
CIGS bottom cell	0.674	18.90	75.7	9.6		
CIGS rear illumination (1 sun)	0.679	23.40	76.1	12.1		
CIGS bottom cell with 20% albedo ($BiFi_{200}$)	0.680	23.28	75.3		11.9	
CIGS bottom cell with 30% albedo ($BiFi_{300}$)	0.678	25.51	74.5		12.9	
Perovskite/CIGS 4-terminal bifacial tandems ($BiFi_{200}$)					**27.0**	**7.9**
Perovskite/CIGS 4-terminal bifacial tandems ($BiFi_{300}$)					**28.0**	**8.9**

Figure 7: Bifacial perovskite/CIGS tandem in four terminal configuration. (a) J-V curves and (b) EQE curves of a perovskite/CIGS bifacial 4-T tandem solar cells as well as of its individual subcells. (c) J-V curves of the CIGS cell as the bottom cell under 0%, 20% and 30% rear albedo illumination. The J-V parameters are also provided in the table.

Recently, bifacial tandem solar cells have drawn a lot of attention due to the best use of the sunlight and better overall performance.[54–56] Especially, all-thin-film bifacial tandem solar cells have many advantages like lighter weight and the potential for roll-to-roll process. Despite thin film CIGS is one of the most promising bottom cells with good long-term stability, low bifacial PCE hindered its development. With a bifacial PCE boost presented in this study, for the first time we demonstrate high performance four terminal bifacial perovskite/CIGS tandem solar cells. The J-V curves and EQE curves are shown in **Fig. 7**. Due to different areas of our perovskite and CIGS cells, the CIGS bottom cells were measured with an optical filter prepared simultaneously with the perovskite top cells, with the same layer sequences and thicknesses. A power generation density of 28.0 mW/cm² $BiFi_{300}$ is obtained, with a power density gain of about 8.9 mW/cm² as compared to the performance of the stand-alone CIGS cell the stand-alone CIGS cell.

A further application of bifacial CIGS cells is all-thin-film 2-terminal bifacial perovskite/CIGS tandem solar devices. With monofacial tandem devices, perovskite with wide-bandgap (> 1.65 eV) are favored to satisfy the current matching condition. However, such layers typically suffer from halide segregation,[57,58] making its long-term stability more challenging. With a bifacial tandem structure, the additional rear illumination can boost the J_{SC} in the bottom cell and satisfy the current matching condition with a perovskite top cell with reduced bandgap. Anticipated high performance and potentially improved stability of bifacial monolithic perovskite/CIGS tandem solar cells could feature a prominent place in future photovoltaics markets.

Conclusion

We have demonstrated a record bifacial CIGS solar cell with efficiencies of 19.77% and 10.89% under the front and rear illumination. A power generation density of 23 mW/cm² $BiFi_{300}$ is foreseen, which is comparable to the CIGS record for mono-facial configuration.

By adding a small amount of Ag (4-5% AAC), absorbers with high quality were obtained with a low-temperature deposition process. The low-temperature process induces a range of benefits to device performance. First, it prevents the formation of detrimental GaO_x at the CIGS/ITO interface, which solves the issues with FF and R_s. Second, it enables the use of µm-thick absorbers with pronounced Ga back gradients. Large gradients help suppress carrier recombination near/at the back interface for high V_{OC} under both front and back illumination, and also increase the penetration depth of light under rear illumination, mitigating carrier loss and boosting J_{SC}. Further, low-temperature processes mitigate the degradation of optical parasitic absorption in the ITO back contact. Overall, the developed process significantly improves the device PCE and J_{SC} under rear illumination, with little to no compromise on device performance under front illumination. However, under rear illumination, J_{SC} remains the bottleneck to higher performance, limited by parasitic absorption losses and non-passivated back contacts.

Finally, we demonstrated the first bifacial perovskite/CIGS tandem device in 4-terminal configuration, achieving power generation densities of 27.0 mW/cm² $BiFi_{200}$ and 28.0 mW/cm² $BiFi_{300}$, respectively. The potential for high performance and improving stability in 2-terminal bifacial perovskite/CIGS tandem devices is also discussed. Last but not least, we report the first direct fabrication (without lift-off process) of a bifacial CIGS device on a flexible substrate. This demonstration is the first step toward technology transfer to roll-to-roll industrial processing. Further improvement in device performance and upscaling development are the next steps for bringing this technology to the commercial market.

Methods

CIGS device fabrication

ITO glass substrates are commercial ones with a 200 nm ITO layer and a SiO_x barrier layer. For CIGS absorbers, a 15 nm Ag layer was deposited by thermal evaporation on the Mo back

contact before absorber deposition. The CIGS absorbers were grown by co-evaporation method with a multi-stage low-temperature deposition process. The shutter of In source was closed in the first 5 minutes of the first stage[23] in order to maximize GGI back gradings. Different nominal depositions temperatures were set for second and third stages, ranging from 453 °C down to 303 °C. The actual substrate temperature is estimated about 30 −50 °C higher than nominal value. After deposition, the absorbers were sequentially treated in-situ with sodium fluoride (NaF) and rubidium fluoride (RbF) post-deposition treatments (PDT) for 20 min each in Se ambient. More details can be found in our previous work.[22] The integrated GGI and [Cu]/([Ga] + [In]) (CGI) values of CIGS absorbers were determined by X-ray fluorescence (XRF), previously calibrated with a reference. The cells were completed with a 30 nm cadmium sulfide (CdS) buffer layer by chemical bath deposition, an RF-sputtered window consisting of 80 nm intrinsic zinc oxide (ZnO) and a 200 nm Al:ZnO (Al_2O_3 2 wt %), electron beam evaporated Ni/Al grids and a MgF_2 anti-reflective coating. Cells of approximately 0.57 cm^2 area were defined by mechanical scribing. Devices on flexible polyimide substrates were processed similarly, except for the ITO deposition by RF-sputtering and cell definition by laser scribing. For ITO on PI foils, a 200 nm ITO was deposited on PI at a flow rate of 59.4 sccm Ar and 0.6 sccm O_2 (0.4 Pa during deposition). The laser scribing process was carried out using a picosecond IR laser source. First, a 135 mW of laser pulse (20 kHz, 3 repetitions) was used to define the cell area (0.40 cm^2) by top TCO isolation. Then, adjacent to the cell area, laser scribes with a pulse of 1.9 W was applied to create a trench to contact the bottom ITO electrode with silver paste.

Perovskite material preparation

Prepatterned indium tin oxide (ITO) coated polyethylene naphthalate (PEN)(12 ohm/sq) were purchased from Advanced Election Technology Co., Ltd. Lead(II) iodide (PbI2, 99.99%), cesium iodide (CsI2, 99%), formamidinium iodide (FAI, ≥99.99%), formamidinium bromide (FABr, ≥99%), methylammonium bromide (MABr, ≥98%), [2-(9H-Carbazol-9-yl)ethyl]phosphonic Acid (2PACz, >98%) were purchased from Tokyo Chemical Industry Co., Ltd. Dimethylformamide (DMF, anhydrous, 99.8%), dimethyl sulfoxide (DMSO, anhydrous, ≥99.9%), dimethyl ether (anhydrous, ≥99.9%), chloroform (CF, anhydrous, 99.8%), isopropa-nol (IPA, anhydrous, ≥99.9%), lead(II) bromide (PbBr2, 99.999%) were purchased from Sig-ma-Aldrich Pty Ltd. Ethanol (anhydrous, ≥99.9%) was purchased from VWR International, LLC. [6,6]-Phenyl-C61-butyric acid methyl ester (PCBM) was purchased from Xi'an Polymer Light Technology Corp. Zinc oxide nanoparticles (ZnO, 2.5 wt% in IPA) were purchased from Avantama AG. All the materials were used as received.

Perovskite top cell fabrication

The pre-patterned PEN/ITO substrates were first cleaned with ethanol and dried with N_2 flow. Then the substrates were further cleaned by UV/Ozone treatment (Jelight Company Inc.) for 20 min. 2PACz precursor (0.3 mg mL^{-1} in ethanol) was spin-coated onto the cleaned ITO sub-strates

at 3000 rpm for 30 s after 1 min's resting on the substrate, followed by an annealing at 100°C for 5 min to remove the solvent. After cooling, perovskite solution was spin-coated on-to the substrate by a two-step spin-coating. The first step is 2000 rpm for 10 s with a ramp-up of 200 rpm s^{-1} and the second step is 6000 rpm for 40 s with a ramp-up of 2000 rpm s^{-1}. Di-ethyl ether (300 μL) was dropped onto the spinning substrate at the 20 s of the second step. The substrate was then annealed at 60°C for 2 min and 100°C for 7 min. The perovskite pre-cursors were prepared by dissolving MABr (21.50 mg), CsI (74.83 mg), FABr (95.98 mg), FAI (198.11 mg), PbBr2 (352.33 mg) and PbI2 (663.85 mg) into a mixed solvent of DMF (1600 μL) and DMSO (400 μL). After cooling, PCBM (20 mg mL^{-1} in chlorofom) was spin-coated at 3000 rpm for 50 s, followed by annealing at 100°C for 10 min. Thereafter, ZnO nanoparticles was spin-coated at 5000 rpm for 50 s, followed by annealing at 100°C for 1 min. All the spin-coating procedures were carried out in N_2-filled glove box. The substrates were then transferred to sputter chamber for the deposition of IZO electrode at a pulsed DC power of 200 W. The active areas of the devices were defined a patterned mask.

Device characterization

J–V curves were measured using a four-terminal Keithley 2400 source meter under standard test conditions (25 °C, 1000 W m^{-2}, AM1.5G illumination, ABA-class sun simulator). EQE was measured using a chopped illumination from a halogen light source, wavelength-selected with a double-grating monochromator. A halogen lamp light bias of about 0.2 sun intensity was applied during the measurements. A certified Si and a calibrated Ge solar cells were used for calibration.

For bifacial device measurements, in addition to one sun illumination from the front side, an additional illumination was provided to the rear side. The intensity of the rear side illumination was calibrated as 0.2 and 0.3 sun by controlling the distance of light-emitting diode (LED) lamp.

The tandem devices in the four-terminal configuration were characterized using a perovskite filter (PEN/ITO/HTL/Perovskite/ETL/ZnO/IZO).

Secondary ion mass spectrometry

Compositional depth profiles were measured by SIMS. The primary beam was 25 keV Bi^+ with total current of 0.6 pA and a raster size of 50×50 μm^2. The sputtering beam was 250 nA, 2 keV O^{2+} with an on-sample area of 300×300 μm^2. GGI depth profiles were determined by scaling the elemental traces with integral GGI values obtained from XRF.

Transmission electron microscopy

TEM cross-sectional samples were prepared by the FEI Helios Nanolab 600i system. High-resolution HAADF-STEM imaging and selected-area electron diffraction have been carried out using a spherical-aberration corrected field emission TEM, JEM-ARM200FTH. Chemical composition analysis by STEM-EDS has been carried out using a F200 HRTEM and Talos F200X.

Ultraviolet-visible spectroscopy

The transmission (T) and reflection (R) spectra were acquired using a ultraviolet–visible-NIR spectrophotometer (Shimadzu UV-3600) equipped with an integrating sphere. Absorption A is calculated using the following formula: A = 1 - T - R

Time-resolved photoluminescence

TRPL measurements were performed using a 639 nm diode laser with 100 ps pulse duration as excitation source, and an InGaAs photomultiplier in combination with a PicoQuant time correlated single photon counting electronics for signal acquisition. Pulse repetition rates were 0.3 MHz. The illumination spot size was around 130 μm diameter. The corresponding photon density was around 3×10^{11} cm^{-2} per pulse. Before TRPL measurements, the window layers were etched away in acetic acid, leaving a thin CdS layer on the absorber.

Data availability

The datasets analysed and generated during the current study are included in the paper and its Supplementary Information. Additional data are available from the corresponding author on reasonable request.

References

(1) Figueres, C.; Schellnhuber, H. J.; Whiteman, G.; Rockström, J.; Hobley, A.; Rahmstorf, S. Three years to safeguard our climate. *Nature* **2017**, *546*, 593–595.

(2) Victoria, M.; Haegel, N.; Peters, I. M.; Sinton, R.; Jäger-Waldau, A.; del Cañizo, C.; Breyer, C.; Stocks, M.; Blakers, A.; Kaizuka, I., et al. Solar photovoltaics is ready to power a sustainable future. *Joule* **2021**, *5*, 1041–1056.

(3) IEA, Solar PV power generation in the Net Zero Scenario, 2000-2030. *Solar-PV* **2021**, https://www.iea.org/data–and–statistics/charts/world–solar–pv–electricity–production–by–region–2005–2019.

(4) Hanmandlu, C.; Chen, C.-Y.; Boopathi, K. M.; Lin, H.-W.; Lai, C.-S.; Chu, C.-W. Bifacial perovskite solar cells featuring semitransparent electrodes. *ACS applied materials & interfaces* **2017**, *9*, 32635–32642.

(5) Jouttijärvi, S.; Lobaccaro, G.; Kamppinen, A.; Miettunen, K. Benefits of bifacial solar cells combined with low voltage power grids at high latitudes. *Renewable and Sustainable Energy Reviews* **2022**, *161*, 112354.

(6) Katsikogiannis, O. A.; Ziar, H.; Isabella, O. Integration of bifacial photovoltaics in agrivoltaic systems: A synergistic design approach. *Applied Energy* **2022**, *309*, 118475.

(7) Kopecek, R.; Libal, J. Towards large-scale deployment of bifacial photovoltaics. *Nature Energy* **2018**, *3*, 443–446.

(8) Kopecek, R.; Libal, J. Bifacial photovoltaics 2021: Status, opportunities and challenges. *Energies* **2021**, *14*, 2076.

(9) ITRPV, International Technology Roadmap for Photovoltaic (ITRPV) - Results 2017. **2018**, https://itrpv.net/Reports/Downloads/.

(10) Nakamura, M.; Yamaguchi, K.; Kimoto, Y.; Yasaki, Y.; Kato, T.; Sugimoto, H. Cd-Free Cu(In,Ga)(Se,S) $_2$ Thin-Film Solar Cell With Record Efficiency of 23.35%. *IEEE J. Photovoltaics* **2019**, *9*, 1863–1867.

(11) EMPA, Press release. **2021**, https://www.empa.ch/web/s604/cigs–efficiency–record–2021.

(12) Shin, M. J.; Lee, A.; Cho, A.; Kim, K.; Ahn, S. K.; Park, J. H.; Yoo, J.; Yun, J. H.; Gwak, J.; Shin, D., et al. Semitransparent and bifacial ultrathin Cu (In, Ga) Se2 solar cells via a single-stage process and light-management strategy. *Nano Energy* **2021**, *82*, 105729.

(13) Nakada, T.; Hirabayashi, Y.; Tokado, T.; Ohmori, D.; Mise, T. Novel device structure for Cu (In, Ga) Se2 thin film solar cells using transparent conducting oxide back and front contacts. *Solar energy* **2004**, *77*, 739–747.

(14) Heinemann, M. D.; Efimova, V.; Klenk, R.; Hoepfner, B.; Wollgarten, M.; Unold, T.; Schock, H.-W.; Kaufmann, C. A. Cu (In, Ga) Se2 superstrate solar cells: prospects and limitations. *Progress in Photovoltaics: Research and Applications* **2015**, *23*, 1228–1237.

(15) Son, Y.-S.; Yu, H.; Park, J.-K.; Kim, W. M.; Ahn, S.-Y.; Choi, W.; Kim, D.; Jeong, J.-h. Control of structural and electrical properties of indium tin oxide (ITO)/Cu (In, Ga) Se2 interface for transparent back-contact applications. *The Journal of Physical Chemistry C* **2019**, *123*, 1635–1644.

(16) Keller, J.; Shariati Nilsson, N.; Aijaz, A.; Riekehr, L.; Kubart, T.; Edoff, M.; Törndahl, T. Using hydrogen-doped In2O3 films as a transparent back contact in (Ag, Cu)(In, Ga) Se2 solar cells. *Progress in Photovoltaics: Research and Applications* **2018**, *26*, 159–170.

(17) Nishimura, T.; Chantana, J.; Mavlonov, A.; Kawano, Y.; Masuda, T.; Minemoto, T. Device design for high-performance bifacial Cu (In, Ga) Se2 solar cells under front and rear illuminations. *Solar Energy* **2021**, *218*, 76–84.

(18) Chen, L.; Lee, J.; Shafarman, W. N. The Comparison of (Ag, Cu)(In,Ga)Se2 and Cu(In,Ga)Se2 Thin Films Deposited by Three-Stage Coevaporation. *IEEE Journal of Photovoltaics* **2013**, *4*, 447–451.

(19) Erslev, P. T.; Lee, J.; Hanket, G. M.; Shafarman, W. N.; Cohen, J. D. The electronic structure of Cu (In1- xGax) Se2 alloyed with silver. *Thin Solid Films* **2011**, *519*, 7296–7299.

(20) Hanket, G. M.; Boyle, J. H.; Shafarman, W. N. Characterization and device performance of (AgCu)(InGa) Se 2 absorber layers. 2009 34th IEEE Photovoltaic Specialists Conference (PVSC). 2009; pp 001240–001245.

(21) Kim, G.; Kim, W. M.; Park, J.-K.; Kim, D.; Yu, H.; Jeong, J.-h. Thin Ag Precursor Layer-Assisted Co-Evaporation Process for Low-Temperature Growth of Cu (In, Ga) Se2 Thin Film. *ACS applied materials & interfaces* **2019**, *11*, 31923–31933.

(22) Yang, S.-C.; Sastre, J.; Krause, M.; Sun, X.; Hertwig, R.; Ochoa, M.; Tiwari, A. N.; Carron, R. Silver-Promoted High-Performance (Ag, Cu)(In, Ga) Se2 Thin-Film Solar Cells Grown at Very Low Temperature. *Solar RRL* **2021**, *5*, 2100108.

(23) Yang, S.-C.; Ochoa, M.; Hertwig, R.; Aribia, A.; Tiwari, A. N.; Carron, R. Influence of Ga back grading on voltage loss in low-temperature co-evaporated Cu (In, Ga) Se2 thin film solar cells. *Progress in Photovoltaics: Research and Applications* **2021**, *29*, 630–637.

(24) Heinemann, M.; Greiner, D.; Unold, T.; Klenk, R.; Schock, H.-W.; Schlatmann, R.; Kaufmann, C. The importance of sodium control in CIGSe superstrate solar cells. *IEEE Journal of Photovoltaics* **2014**, *5*, 378–381.

(25) Ochoa, M.; Nishiwaki, S.; Yang, S.-C.; Tiwari, A. N.; Carron, R. Lateral Charge Carrier Transport in Cu (In, Ga) Se2 Studied by Time-Resolved Photoluminescence Mapping. *physica status solidi (RRL)–Rapid Research Letters* **2021**, *15*, 2100313.

(26) Nakada, T.; Hirabayashi, Y.; Tokado, T. Cu (In1-x, Gax) Se2-based thin film solar cells using transparent conducting back contacts. *Japanese Journal of Applied Physics* **2002**, *41*, L1209.

(27) Carron, R.; Nishiwaki, S.; Feurer, T.; Hertwig, R.; Avancini, E.; Löckinger, J.; Yang, S.-C.; Buecheler, S.; Tiwari, A. N. Advanced Alkali Treatments for High-Efficiency Cu(In,Ga)Se2 Solar Cells on Flexible Substrates. *Advanced Energy Materials* **2019**, *9*, 1900408.

(28) Keller, J.; Chen, W.-C.; Riekehr, L.; Kubart, T.; Törndahl, T.; Edoff, M. Bifacial Cu (In, Ga) Se2 solar cells using hydrogen-doped In2O3 films as a transparent back contact. *Progress in Photovoltaics: Research and Applications* **2018**, *26*, 846–858.

(29) Pokaipisit, A.; Horprathum, M.; Limsuwan, P. Influence of oxygen flow rate on properties of indium tin oxide thin films prepared by ion-assisted electron beam evaporation. *Sonklanakarin Journal of Science and Technology* **2009**, *31*, 577.

(30) Ren, Y.; Liu, P.; Liu, R.; Wang, Y.; Wei, Y.; Jin, L.; Zhao, G. The key of ITO films with high transparency and conductivity: Grain size and surface chemical composition. *Journal of Alloys and Compounds* **2022**, *893*, 162304.

(31) Carron, R.; Avancini, E.; Feurer, T.; Bissig, B.; Losio, P. A.; Figi, R.; Schreiner, C.; Bürki, M.; Bourgeois, E.; Remes, Z., et al. Refractive indices of layers and optical simulations of Cu (In, Ga) Se2 solar cells. *Science and Technology of advanced MaTerialS* **2018**, *19*, 396–410.

(32) Chang, Y.-H.; Carron, R.; Ochoa, M.; Bozal-Ginesta, C.; Tiwari, A. N.; Durrant, J. R.; Steier, L. Insights from Transient Absorption Spectroscopy into Electron Dynamics Along the Ga-Gradient in Cu (In, Ga) Se2 Solar Cells. *Advanced Energy Materials* **2021**, *11*, 2003446.

(33) Jiang, Y.; Feurer, T.; Carron, R.; Sevilla, G. T.; Moser, T.; Pisoni, S.; Erni, R.; Rossell, M. D.; Ochoa, M.; Hertwig, R., et al. High-mobility In2O3: H electrodes for four-terminal perovskite/CuInSe2 tandem solar cells. *ACS nano* **2020**, *14*, 7502–7512.

(34) Mavlonov, A.; Chantana, J.; Nishimura, T.; Kawano, Y.; Inoue, M.; Hamada, N.; Masuda, T.; Minemoto, T. Superstrate-type flexible and bifacial Cu (In, Ga) Se2 thin-film solar cells with In2O3: SnO2 back contact. *Solar Energy* **2020**, *211*, 725–731.

(35) Nishimura, T.; Hamada, N.; Chantana, J.; Mavlonov, A.; Kawano, Y.; Masuda, T.; Minemoto, T. Application of two-dimensional MoSe2 atomic layers to the lift-off process for producing light-weight and flexible bifacial Cu (In, Ga) Se2 solar cells. *ACS Applied Energy Materials* **2020**, *3*, 9504–9508.

(36) Mavlonov, A.; Nishimura, T.; Chantana, J.; Kawano, Y.; Minemoto, T. Effect of an Ohmic back contact on the stability of Cu (In, Ga) Se2-based flexible bifacial solar cells. *Applied Physics Letters* **2021**, *119*, 103903.

(37) Hamada, N.; Nishimura, T.; Chantana, J.; Kawano, Y.; Masuda, T.; Minemoto, T. Fabrication of flexible and bifacial Cu (In, Ga) Se2 solar cell with superstrate-type structure using a lift-off process. *Solar Energy* **2020**, *199*, 819–825.

(38) Mavlonov, A.; Nishimura, T.; Chantana, J.; Kawano, Y.; Masuda, T.; Minemoto, T. Back-contact barrier analysis to develop flexible and bifacial Cu (In, Ga) Se2 solar cells using transparent conductive In2O3: SnO2 thin films. *Solar Energy* **2020**, *211*, 1311–1317.

(39) McClelland, R.; Fan, J.; Gale, R.; Dingle, B. High-efficiency thin-film GaAs bifacial solar cells. IEEE Conference on Photovoltaic Specialists. 1990; pp 145–147.

(40) Shin, M. J.; Park, S.; Lee, A.; Park, S. J.; Cho, A.; Kim, K.; Ahn, S. K.; Park, J. H.; Yoo, J.; Shin, D., et al. Bifacial photovoltaic performance of semitransparent ultrathin Cu (In, Ga) Se2 solar cells with front and rear transparent conducting oxide contacts. *Applied Surface Science* **2021**, *535*, 147732.

(41) Mazzer, M.; Rampino, S.; Spaggiari, G.; Annoni, F.; Bersani, D.; Bissoli, F.; Bronzoni, M.; Calicchio, M.; Gombia, E.; Kingma, A., et al. Bifacial CIGS solar cells grown by low temperature pulsed electron deposition. *Solar Energy Materials and Solar Cells* **2017**, *166*, 247–253.

(42) Cavallari, N.; Pattini, F.; Rampino, S.; Annoni, F.; Barozzi, M.; Bronzoni, M.; Gilioli, E.; Gombia, E.; Maragliano, C.; Mazzer, M., et al. Low temperature deposition of bifacial CIGS solar cells on Al-doped Zinc Oxide back contacts. *Applied Surface Science* **2017**, *412*, 52–57.

(43) Kim, D.; Shin, S. S.; Lee, S. M.; Cho, J.-S.; Yun, J. H.; Lee, H. S.; Park, J. H. Flexible and semi-transparent ultra-thin CIGSe solar cells prepared on ultra-thin glass substrate: a key to flexible bifacial photovoltaic applications. *Advanced Functional Materials* **2020**, *30*, 2001775.

(44) Romeo, A.; Khrypunov, G.; Galassini, S.; Zogg, H.; Tiwari, A. Bifacial configurations for CdTe solar cells. *Solar energy materials and solar cells* **2007**, *91*, 1388–1391.

(45) Subedi, K. K.; Phillips, A. B.; Shrestha, N.; Alfadhili, F. K.; Osella, A.; Subedi, I.; Awni, R. A.; Bastola, E.; Song, Z.; Li, D.-B., et al. Enabling bifacial thin film devices by developing a back surface field using CuxAlOy. *Nano Energy* **2021**, *83*, 105827.

(46) Marsillac, S.; Parikh, V.; Compaan, A. Ultra-thin bifacial CdTe solar cell. *Solar energy materials and solar cells* **2007**, *91*, 1398–1402.

(47) Lohmüller, E.; n èe Werner, S. L.; Norouzi, M. H.; Saint-Cast, P.; Weber, J.; Meier, S.; Wolf, A. Towards 90% bifaciality for p-type Cz-Si solar cells by adaption of industrial PERC processes. 2018 IEEE 7th World Conference on Photovoltaic Energy Conversion (WCPEC)(A Joint Conference of 45th IEEE PVSC, 28th PVSEC & 34th EU PVSEC). 2018; pp 3727–3731.

(48) Ohtsuka, H.; Sakamoto, M.; Tsutsui, K.; Yazawa, Y. Bifacial silicon solar cells with 21 · 3% front efficiency and 19 · 8% rear efficiency. *Progress in Photovoltaics: Research and Applications* **2000**, *8*, 385–390.

(49) Moehlecke, A.; Zanesco, I.; Luque, A. Practical high efficiency bifacial solar cells. Proceedings of 1994 IEEE 1st World Conference on Photovoltaic Energy Conversion-WCPEC (A Joint Conference of PVSC, PVSEC and PSEC). 1994; pp 1663–1666.

(50) Hübner, A.; Aberle, A. G.; Hezel, R. Novel cost-effective bifacial silicon solar cells with 19.4% front and 18.1% rear efficiency. *Applied physics letters* **1997**, *70*, 1008–1010.

(51) Song, Z.; Chen, C.; Li, C.; Rijal, S.; Chen, L.; Li, Y.; Yan, Y. Assessing the true power of bifacial perovskite solar cells under concurrent bifacial illumination. *Sustainable Energy & Fuels* **2021**, *5*, 2865–2870.

(52) Najafi, M.; Zardetto, V.; Zhang, D.; Koushik, D.; Dörenkämper, M. S.; Creatore, M.; Andriessen, R.; Poodt, P.; Veenstra, S. Highly efficient and stable semi-transparent p-i-n planar perovskite solar cells by atmospheric pressure spatial atomic layer deposited ZnO. *Solar Rrl* **2018**, *2*, 1800147.

(53) Wang, H.; Dewi, H. A.; Koh, T. M.; Bruno, A.; Mhaisalkar, S.; Mathews, N. Bifacial, color-tunable semitransparent perovskite solar cells for building-integrated photovoltaics. *ACS applied materials & interfaces* **2019**, *12*, 484–493.

(54) Kim, S.; Trinh, T. T.; Park, J.; Pham, D. P.; Lee, S.; Do, H. B.; Dang, N. N.; Dao, V.-A.; Kim, J.; Yi, J. Over 30% efficiency bifacial 4-terminal perovskite-heterojunction silicon tandem solar cells with spectral albedo. *Scientific Reports* **2021**, *11*, 1–10.

(55) De Bastiani, M.; Mirabelli, A. J.; Hou, Y.; Gota, F.; Aydin, E.; Allen, T. G.; Troughton, J.; Subbiah, A. S.; Isikgor, F. H.; Liu, J., et al. Efficient bifacial monolithic perovskite/silicon tandem solar cells via bandgap engineering. *Nature Energy* **2021**, *6*, 167–175.

(56) Coletti, G.; Luxembourg, S. L.; Geerligs, L.; Rosca, V.; Burgers, A.; Wu, Y.; Okel, L.; Kloos, M.; Danzl, F.; Najafi, M., et al. Bifacial four-terminal perovskite/silicon tandem solar cells and modules. *ACS Energy Letters* **2020**, *5*, 1676–1680.

(57) Xu, J.; Boyd, C. C.; Yu, Z. J.; Palmstrom, A. F.; Witter, D. J.; Larson, B. W.; France, R. M.; Werner, J.; Harvey, S. P.; Wolf, E. J., et al. Triple-halide wide–band gap perovskites with suppressed phase segregation for efficient tandems. *Science* **2020**, *367*, 1097–1104.

(58) Jošt, M.; Kegelmann, L.; Korte, L.; Albrecht, S. Monolithic perovskite tandem solar cells: A review of the present status and advanced characterization methods toward 30% efficiency. *Advanced Energy Materials* **2020**, *10*, 1904102.

Acknowledgement

This work has received funding from the Swiss Federal Office of Energy (SFOE) (SI/502310-01 "ACIGS"). This work was partially supported by Young Scholar Fellowship Einstein Program of MOST, Taiwan (grant no. MOST 110-2636-E-007-015) Huagui Lai thanks the funding of China Scholarship Council (CSC) from the Ministry of Education of P. R. China. This project has received funding from the European Union's Horizon 2020 research and innovation programme under grant agreement N° 850937. The work also acknowledges the financial support from the Strategic Focus Area Advanced Manufacturing under the project AMYS - Advancing manufacturability of hybrid organic-inorganic semiconduc-tors for large area optoelectronics.

The authors gratefully acknowledge the use of UHRTEM (Dr. Chong-Chi Chi) and HRTEM (Ms. Yi-Jen Yu) equipment belonging to the Instrumentation Center at National Tsing Hua University in Taiwan and FIB (Dr. Wei-Ni Lee) at CNMM of the National Tsing Hua University in Taiwan.

Competing interests

The authors declare no competing interests.

Author contributions

S-C.Y. proposed the research. R.C. and A.N.T. supervised the work. S-C.Y. designed the experiments, fabricated all devices and conducted the characterization. T-Y.L. carried out the STEM and TEM measurements. M.O. and R.C. performed optical and numerical simulation. H.L. assisted the characterization for bifacial and tandem measurements. R.K. performed laser scribing on PI samples. F.F. supported on experimental and characterization designs. S-C.Y. wrote the manuscript with input from all other co-authors.

Additional information

Supplementary information

The online version contains supplementary material available at XXX